JOURNAL OF PROPULSION AND POWER
Vol. 24, No. 1, January–February 2008

Computational Study of the Propulsive Characteristics of a Shcramjet Engine

Derrick C. Alexander* and Jean P. Sislian†
University of Toronto, Toronto, Ontario M3H 5T6, Canada

DOI: 10.2514/1.29951

A shock-induced combustion ramjet is considered wherein gaseous hydrogen is injected via cantilevered ramp injectors located in a staggered manner on opposite walls of the internal duct of a mixed-compression inlet. The nonhomogeneous combustible mixture thus formed at the exit of the duct is then ignited through a shock generated by a wedge located on the lower wall of the duct. The products of the ensuing combustion process are then expanded in a specifically designed nozzle. The numerical simulation of the three-dimensional shcramjet flowfield at Mach 11 and an altitude of 34.5 km is performed by the Window Allocatable Resolver for Propulsion code, in which the multispecies Favre-averaged Navier–Stokes equations are closed by the k-ω turbulence model and the Wilcox dilatational dissipation correction, to account for compressibility effects at high convective Mach number. The H_2–air chemical reactions are modeled by a nine species, 20 reaction model based on that of Jachimowski. Magnitudes of the thrust, fuel specific impulse, and frictional forces on the entire shcramjet configuration are numerically determined. The moderate value of fuel specific impulse of 683 s is primarily due to the high equivalence ratio adopted.

Nomenclature

c_k = mass fraction of species k
c_p = specific heat at constant pressure
D_k = mass diffusion coefficient of species k
d_w = distance from wall to first inner node
E = total specific energy, $e + k + 1/2q^2$
e = specific internal energy
$\boldsymbol{F}_i$ = convection flux vector in the i direction
$\mathcal{F}_{\text{pot}}$ = specific thrust potential
$\mathcal{F}_p$ = pressure force
$\mathcal{F}_{\text{friction}}$ = frictional force
$\mathcal{F}_{\text{fuel}}$ = fuel thrust
$\boldsymbol{G}$ = vector of diffusion variables
h_k = enthalpy of species k
I_{sp} = specific impulse
J = metric Jacobian
$\mathbf{K}_{i,j}$ = diffusion matrix
k = turbulent kinetic energy
M_T = turbulent Mach number, $\sqrt{2k}/a$
$\dot{m}$ = mass flow rate
nd = number of dimensions
ns = number of species
P_k = production of turbulent kinetic energy
Pr_T = turbulent Prandtl number
p = pressure
p^* = effective pressure, $p + 2/3\rho k$
$\mathbf{Q}$ = conserved variables
q = magnitude of velocity vector
$\mathbf{R}$ = residual
$\mathbf{S}$ = source terms
Sc_T = turbulent Schmidt number
T = temperature
V_i = contravariant velocity
v_i = velocity component in the i direction
$\dot{W}_k$ = chemical production rate of species k
X_i = curvilinear coordinate in the i direction
$X_{i,j}$ = $\partial X_i/\partial x_j$
x_i = Cartesian coordinate in the i direction
y^+ = nondimensional wall distance, $d_w\rho\sqrt{\tau_w/\rho_w}/\mu$
$\beta_{i,j}^{r,s}$ = $\alpha_{i,j}\delta_{r,s} + J^{-1}X_{i,s}X_{j,r} - 2/3J^{-1}X_{i,r}X_{j,s}$
Γ = circulation
δ_{ij} = Kronecker delta
δ_{X_i} = discrete derivative with respect to X_i
η_m = mixing efficiency
κ = thermal conductivity
μ = viscosity
μ_T = turbulent eddy viscosity
ξ = convergence criterion
ρ = density
σ_k = Wilcox turbulent closure coefficient
σ_ω = Wilcox turbulent closure coefficient
τ = pseudotime
τ_w = wall shear stress
ω = dissipation rate per unit of turbulent kinetic energy

Received 24 January 2007; revision received 8 May 2007; accepted for publication 6 June 2007.

*Postdoctoral Fellow, Institute for Aerospace Studies; derrick@caius.utias.utoronto.ca. Member AIAA.

†Professor, Institute for Aerospace Studies; sislian@caius.utias.utoronto.ca. Associate Fellow AIAA.

Introduction

THE practical implementation of the shock-induced combustion ramjet (shcramjet) concept for hypersonic flight is contingent upon the feasibility of quasi-homogeneous fuel/air mixing in the high-velocity, high-temperature forebody (inlet) air flow of the vehicle. Simultaneously premature ignition of the combustible mixture everywhere upstream of the combustion-inducing shock must be avoided. In [1,2], an attempt has been made to devise such premixing in a generic, two shock, external-compression inlet. Because the shcramjet concept is considered as an alternative to the scramjet for very high flight Mach numbers, the premixing task in the inlet was considered at a flight Mach number of 11. Cantilevered ramp fuel injectors located at the tip of the inlet were used to inject the fuel (gaseous hydrogen). An air-based mixing efficiency of 0.41 was obtained just before the combustion process, with premature ignition of the combustible mixture in the boundary layer occurring in the last 15% of the inlet length. Subsequent ignition of the nonhomogeneous combustible mixture by an oblique shock wave resulted in a fuel specific impulse of approximately 573 s, based on the concept of thrust potential. The relatively low values of mixing efficiency and of specific impulse, as well as the occurrence of premature ignition in the inlet boundary layer, were attributed to the adverse effects of the flowfield characteristics on the mixing process in the generic

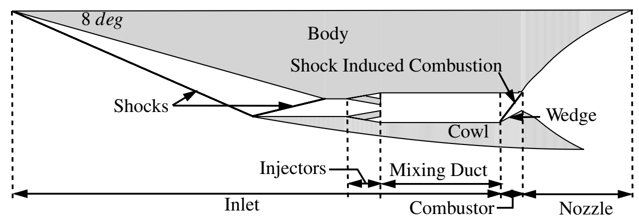

Fig. 1 Mixed-compression inlet shcramjet schematic.

external-compression inlet model considered. It should be noted that the concept of liquid-hydrocarbon fuel preinjection in the forebody flow of a hypersonic engine has lately gained interest with a view to improve the combustion efficiency of scramjets in the flight Mach number range of 3.5–8. A complete review of this round of investigations is given in [3].

To alleviate the aforementioned shortcomings of the shcramjet model considered in [1,2], an alternative shcramjet model is considered in the present paper wherein the fuel is injected by cantilevered ramp injectors placed in a staggered manner on the upper and lower walls at the upstream end of the internal duct of the mixed-compression inlet, Fig. 1. A detailed numerical study of such a fuel/air premixing configuration is given in [4,5], where it was shown that for approximately the same order of magnitude of air and fuel velocities in the duct as in [1], an air-based mixing efficiency of 0.68 can be obtained. Injector configurations were found such that the combustible mixture was well away from the confining walls of the duct and no premature ignition was present.

Unlike [2], where only the premixing process in the external-compression inlet and the combustor flowfield were numerically simulated, the present study reports results of a numerical simulation of a complete, *integrated*, three-dimensional shcramjet flowfield. The premixed combustible mixture in the mixed-compression inlet, similar to those considered in [4], is ignited by a shock-inducing wedge located on the lower body wall of the internal duct of the inlet at a distance of 0.8 m from the point of fuel injection. The products of the ensuing shock-induced combustion process are expanded in a specifically designed nozzle. Magnitudes of the thrust, fuel specific impulse, and frictional forces acting on the entire shcramjet model are numerically determined.

Governing Equations

The shcramjet flowfield is described by the Favre-averaged Navier–Stokes equations, closed by the k-ω turbulence model of Wilcox [6] and the nine species, 20 reaction Jachimowski H_2/air chemical model [7] (nitrogen is assumed to be an inert gas). The equations are expressed in generalized coordinates as $\partial \mathbf{Q}/\partial\tau = -\mathbf{R}$, where minimization of the residual is sought.

$$\mathbf{R} = \sum_{i=1}^{\mathrm{nd}}\left[\frac{\partial \boldsymbol{F}_i}{\partial X_i} - \sum_{j=1}^{\mathrm{nd}}\frac{\partial}{\partial X_i}\left(\mathbf{K}_{i,j}\frac{\partial \boldsymbol{G}}{\partial X_j}\right)\right] - \mathbf{S} \tag{1}$$

For the conservative variable, convective flux, and diffusion term, we have

$$\mathbf{Q} = \frac{1}{J}\begin{bmatrix} \rho c_1 \\ \vdots \\ \rho c_{\mathrm{ns}} \\ \rho v_1 \\ \vdots \\ \rho v_{\mathrm{nd}} \\ \rho E \\ \rho k \\ \rho\omega \end{bmatrix}, \qquad \boldsymbol{F}_i = \frac{1}{J}\begin{bmatrix} \rho V_i c_1 \\ \vdots \\ \rho V_i c_{\mathrm{ns}} \\ \rho V_i v_1 + X_{i,1}p^\star \\ \vdots \\ \rho V_i v_{\mathrm{nd}} + X_{i,\mathrm{nd}}p^\star \\ \rho V_i E + V_i p^\star \\ \rho V_i k \\ \rho V_i \omega \end{bmatrix}, \qquad \boldsymbol{G} = \begin{bmatrix} c_1 \\ \vdots \\ c_{\mathrm{ns}} \\ v_1 \\ \vdots \\ v_{\mathrm{nd}} \\ T \\ k \\ \omega \end{bmatrix} \tag{2}$$

where

$$V_i = \sum_{m=1}^{\mathrm{nd}} X_{i,m} v_m$$

is the contravariant velocity. The total energy and effective pressure include molecular and turbulent components, $E = e + k + 1/2q^2$ and $p^\star = p + 2/3\rho k$. The internal energy, enthalpy, and specific heat at constant pressure are determined from temperature dependent polynomials from McBride and Reno [8], whereas p is found through the ideal gas law from the temperature and density. With

$$\alpha_{i,j} = J^{-1}\sum_{m=1}^{\mathrm{nd}} X_{i,m}X_{j,m}$$

the diffusion matrix can be shown to be

$$\mathbf{K}_{i,j} = \begin{bmatrix} \alpha_{i,j}D_1^\star & \cdots & 0 & 0 & \cdots & 0 & 0 & 0 & 0 \\ \vdots & \ddots & \vdots & \vdots & \ddots & \vdots & \vdots & \vdots & \vdots \\ 0 & \cdots & \alpha_{i,j}D_{\mathrm{ns}}^\star & 0 & \cdots & 0 & 0 & 0 & 0 \\ 0 & \cdots & 0 & \mu^\star\beta_{i,j}^{1,1} & \cdots & \mu^\star\beta_{i,j}^{1,\mathrm{nd}} & 0 & 0 & 0 \\ \vdots & \ddots & \vdots & \vdots & \ddots & \vdots & \vdots & \vdots & \vdots \\ 0 & \cdots & 0 & \mu^\star\beta_{i,j}^{\mathrm{nd},1} & \cdots & \mu^\star\beta_{i,j}^{\mathrm{nd},\mathrm{nd}} & 0 & 0 & 0 \\ \alpha_{i,j}h_1D_1^\star & \cdots & \alpha_{i,j}h_{\mathrm{ns}}D_{\mathrm{ns}}^\star & \mu^\star\sum_{k=1}^{\mathrm{ns}} v_k\beta_{i,j}^{k,1} & \cdots & \mu^\star\sum_{k=1}^{\mathrm{ns}} v_k\beta_{i,j}^{k,\mathrm{nd}} & \alpha_{i,j}\kappa^\star & \alpha_{i,j}\mu_k^\star & 0 \\ 0 & \cdots & 0 & 0 & \cdots & 0 & 0 & \alpha_{i,j}\mu_k^\star & 0 \\ 0 & \cdots & 0 & 0 & \cdots & 0 & 0 & 0 & \alpha_{i,j}\mu_\omega^\star \end{bmatrix} \tag{3}$$

For the effective viscosity, thermal conductivity, mass diffusion, and diffusion coefficients of the turbulent kinetic energy and length scale determining equations, we have $\mu^\star = \mu + \mu_T$, $\kappa^\star = \kappa + c_p\mu_T/Pr_T$, $D_k^\star = D_k + \mu_T/Sc_T$, $\mu_k^\star = \mu + \mu_T/\sigma_k$, and $\mu_\omega^\star = \mu + \mu_T/\sigma_\omega$. Based on dimensional analysis arguments, the turbulent viscosity can be written as $\mu_T = 0.09\rho k/\omega$. The turbulent Prandtl number, σ_k, and σ_ω are set to 0.9, 2.0, and 2.0, respectively, whereas the turbulent Schmidt number is set to 1.0 and not altered in space. The source term includes the chemical species production terms, the baseline terms of the k-ω model, as well as additional terms needed to account for compressibility effects.

$$\mathbf{S} = \frac{1}{J}\begin{bmatrix} \dot{W}_1 \\ \vdots \\ \dot{W}_{\mathrm{ns}} \\ 0 \\ \vdots \\ 0 \\ 0 \\ P_k - \rho k\omega - \rho k\omega f(M_T) \\ \frac{\omega}{k}\left(\frac{5}{9}P_k + \frac{5}{6}\rho k\omega\right) + \rho\omega^2 f(M_T) \end{bmatrix} \tag{4}$$

The dilatational dissipation correction terms [that is, the ones involving $f(M_T)$] are necessary to account for the reduced growth of shear layers when the convective Mach number is high [9,10]. The Wilcox [11] dilatational dissipation model specifies $f(M_T) = 3/2\max(0, M_T^2 - 1/16)$. This improves the baseline k-ω equations in solving high convective Mach number shear layers without underpredicting the skin friction in high Mach number boundary layers, at least up to a freestream Mach number of six. More compressible corrections exist [12], but due to very little or no empirical data to justify their presence, their effect is neglected in the present study. From the exact form of the transport equation for k, the turbulent kinetic energy production term can be written in generalized coordinates as

$$P_k = \sum_{i=1}^{\mathrm{nd}}\sum_{j=1}^{\mathrm{nd}}\left(-\frac{2}{3}\rho k X_{i,j}\frac{\partial v_j}{\partial X_i} + \mu^\star \sum_{m=1}^{\mathrm{nd}}\sum_{n=1}^{\mathrm{nd}} J\beta_{i,j}^{m,n}\frac{\partial v_n}{\partial X_j}\frac{\partial v_m}{\partial X_i}\right) \tag{5}$$

Numerical Method

The discretized governing equations together with the boundary conditions are solved on a generalized structured mesh using the Window Allocatable Resolver for Propulsion (WARP) code. A detailed description of the computational technique employed in the WARP code can be found in [13]. All partial derivatives are discretized using second-order accurate, centered finite difference stencils except for the convection derivative, which is discretized using the approximate Riemann solver of Roe [14] and made second-order accurate through a symmetric minmod limiter by Yee et al. [15]. The discretized residual is solved to steady state using a block-implicit factorization algorithm [16] including the analytical Jacobian derived from the chemical model and a linearization strategy of the viscous terms by Chang and Merkle [17]:

$$\prod_{i=1}^{\mathrm{nd}}\left[I + \Delta\tau\delta_{X_i}\frac{\partial \boldsymbol{F}_i}{\partial \mathbf{Q}} - \Delta\tau\delta_{X_i}(\mathbf{K}_{i,i}\delta_{X_i}\mathbf{B}) - \delta_{1,i}\Delta\tau\mathbf{C}^-\right]\Delta\mathbf{Q} = -\Delta\tau\mathbf{R}_\Delta \tag{6}$$

with $\mathbf{B} \equiv \partial\boldsymbol{G}/\partial\mathbf{Q}$ the linearization Jacobian of the viscous terms and $\mathbf{C}^- \equiv \partial\mathbf{S}^-/\partial\mathbf{Q}$ the linearization Jacobian of the chemical and negative turbulent source terms. Only the negative turbulent source terms are linearized to ensure the stability of the implicit algorithm. The term $\delta_{X_i}\partial\boldsymbol{F}_i/\partial\mathbf{Q}$ is determined by the linearization of the first-order Roe scheme with the Roe Jacobian locally frozen [18,19]. Although more costly per iteration compared with a lower-upper symmetric Gauss–Seidel inversion strategy, approximate factorization is chosen here for its ability to solve the Roe scheme without the need for introducing an explicit artificial dissipation term in the residual (the entropy correction) to stabilize the iterative process. The introduction of the entropy correction adds additional artificial dissipation to the numerical scheme, which affects the accuracy of the solution considerably [20].

The quantity ξ is defined as the maximum between the sum of the discretized continuity residuals and the energy conservation residual divided by $\mathbf{Q}$:

$$\xi \equiv \max\left(\frac{\sum_{k=1}^{\mathrm{ns}}|\mathbf{R}_{\Delta,k}|}{J^{-1}\rho}, \frac{|\mathbf{R}_{\Delta,\mathrm{ns}+\mathrm{nd}+1}|}{J^{-1}\rho E}\right) \tag{7}$$

For all cases considered, ξ decreases through at least five orders of magnitude and convergence is reached when ξ for all nodes falls below $\xi_{\mathrm{converge}} = 400\ \mathrm{s}^{-1}$. The pseudo-time-step $\Delta\tau$ is fixed to the geometric average between the minimum and maximum Courant–Friedrichs–Lewy (CFL) conditions, which is found to give faster convergence than the minimum CFL condition for cases involving high mesh aspect ratios.

The WARP code uses a "marching window" technique that detects, without user interference, the hyperbolic or elliptic character of the considered flow using an "ellipticity sensor" that is based on the eigenvalue signs of the streamwise convective flux Jacobian, and unlike other similar techniques used so far, is valid for viscous streamwise separated flows. The algorithm performs localized pseudo-time-stepping on a subdomain composed of a sequence of streamwise planes that advances in the streamwise direction when the residual of the upstream boundary of the subdomain falls below the convergence threshold. The width of the marching window decreases to only a few planes in regions of quasi-hyperbolic flow and increases to the size of the streamwise-elliptic region when encountered. The marching window is strictly a convergence acceleration technique, as it guarantees the nodes upstream of the window are below the convergence threshold by updating the residual upstream of the window at all pseudo-time-steps. This method captures all upstream propagating waves significantly affecting the residual. Compared with the standard pseudo-time-marching approach, the marching window decreases the time required for convergence by up to 25 times for flows with little streamwise ellipticity and up to eight times for flows with large streamwise separated regions. Storage is reduced by up to six times by not allocating memory to the nodes not included in the considered computational subdomain. A full description of this method, its implementation in WARP, and validation of its ability to capture elliptical phenomena can be found in [13].

The WARP code has been validated against the following experimental data obtained for a number of hypervelocity flows similar to those simulated herein: Settles et al. [21] shock wave/turbulent boundary-layer interaction at $M = 2.84$, Burrows and Kurkov's [22] wall fuel injection mixing and combusting flowfield, Waitz et al. [23] Mach 6 fuel/air mixing by a ramp injector, Donohue et al. [24] Mach 2 swept ramp injector mixing problem, Mao et al. [25] Mach 3 wall fuel injection at a 15 deg angle, and Lehr's [26] blunt-body detonation and shock-induced combustion in a Mach 5 stoichiometric H_2/air flow. In all cases considered, agreement of the numerical predictions were well within limits acceptable in the hypersonic propulsion research community. For more details on the validation effort and the various levels of agreement, see [4,27].

A three-dimensional domain is used for the internal engine flow, which is subdivided into the internal duct portion of the inlet, the combustor, and the nozzle regions. The use of the marching window technique allows the three-dimensional domain to be solved on streamwise subdomains that yield a solution of the entire engine flowfield, which is physically the same as solving the entire domain, as long as the subdomain grids overlap and no significant phenomena that increase the residual are observed to be traveling upstream to the start of the computational subdomains. The structured grid in all regions is body-fitted and clustered to appropriately capture the boundary layers and sharp corners, including that of the injectors and aerodynamic wedge. The grid cross section maintains the same dimensions throughout the engine, with 248 cells in the vertical x_2 direction and 105 cells in the spanwise x_3 direction. The flow over the flat top of the entire engine, the external-compression inlet surface, and the initial portion of the external surface of the cowl are treated as two-dimensional.

Boundary Conditions

The assumption is made that infinite spanwise fuel injector arrays are representative of the fuel/air mixing process away from the sidewalls of the engine. Hence, second-order symmetry conditions were imposed on the spanwise sides of the computational domain that lie along the centerline of adjacent staggered injectors on opposite walls, at $x_3 = 0.00$ and $x_3 = 0.03$ m. Subsequent combustor and nozzle domains retain the same computational span. The initial x_1 boundary plane of the subdomains were specified as supersonic inflow and the end boundary plane as a zeroth order supersonic outflow. All wall surfaces in the propulsive duct are assumed to be no-slip, noncatalytic, and cooled to an arbitrarily chosen constant 500 K with values at the walls determined by a second-order extrapolation from the interior flow. At the wall, $k = 0$, whereas the specific dissipation rate $\omega = 36\mu/5\rho d_w^2$, as given by Wilcox [6]. To maintain practical grid sizes, node spacing at the wall surfaces is $d_w = 10$ μm. For integration through the laminar sublayer, Wilcox has suggested y^+ should be less than one [28].

Freestream Conditions

In the Wilcox k-ω model [6], the turbulent kinetic energy is set to a small value in the freestream to prevent division by zero in the dissipation rate source term, Eq. (4). However, in the present study, in the freestream, $k = 0$ and $\tilde{k}$ is defined as

$$\tilde{k} = \max\left[k, \min\left(k_{\mathrm{div}}, \frac{\omega\mu}{\rho}\right)\right] \tag{8}$$

with k_{div} a user-specified constant that is generally set lower than one-tenth of the maximum value of k throughout the boundary layer [13]. This is verified numerically not to affect the laminar sublayer, but to improve the robustness and efficiency of the integration significantly. The minimum between k_{div} and $\omega\mu/\rho$ is taken so that a clipping occurs *only* in nonturbulent flow regions in which an accurate representation of ω does not affect the accuracy of the flowfield. A value of k_{div} of 1000 $\mathrm{m^2/s^2}$ is used for all cases and is verified to be below the maximum value of k in the boundary layer, which for the present case is between 40,000 and 70,000 $\mathrm{m^2/s^2}$. The freestream ω is set to 10 $\mathrm{m^{-1}}$ times the freestream velocity as suggested by Wilcox, which is 100–1000 times smaller than the maximum ω value present at all x_1 planes.

Global Performance Parameters

A measure of the intensity of vortices generated by the cantilevered ramp fuel injectors and their subsequent variation along the engine, which reflect the extent of fuel/air mixing, is provided by the concept of circulation, expressed as the integral of the vorticity field over any x_1 plane of interest (subscript b). Because vortices may have opposite rotations and hence reduce the circulation, the absolute circulation is used to provide an estimate of the total vorticity in the cross section.

$$|\Gamma| = \frac{1}{A_b}\int_b \left|\frac{\partial v_3}{\partial x_2} - \frac{\partial v_2}{\partial x_3}\right| \mathrm{d}A \tag{9}$$

where A_b is the area of the cross-sectional plane b.

The concept of mixing efficiency quantifies the fuel/air mixing process. The *air-based* mixing efficiency η_m, at a streamwise plane of interest (denoted by subscript b), is defined as the ratio of the oxygen that would burn in the plane to the mass flux of oxygen entering the engine.

$$\eta_m = \int_b c_{O_2}^R \,\mathrm{d}\dot{m}/(0.234 \times \dot{m}_{\mathrm{air,engine}}) \tag{10}$$

The mass fraction of reacting oxygen $c_{O_2}^R$ is given as

$$c_{O_2}^R = \min\left(c_{O_2}, c_{O_2}^S \cdot c_{H_2}/c_{H_2}^S\right) \tag{11}$$

with the stoichiometric mass fraction of oxygen $c_{O_2}^S$ equal to 0.2284, and the stoichiometric mass fraction of hydrogen $c_{H_2}^S$ equal to 0.02876. Note that this formulation does not take into account the flammability limits of hydrogen in air, which are $0.1 < \phi < 7.0$ at standard pressure and have been shown to lie above $\phi = 0.8$ for cases similar to the ones studied here [29].

Because the propulsive flow is subject to significant total temperature variations, the conventional measure of loss assessment by the mass flux averaged total pressure is not indicative of the real losses incurred in various components of the engine and, therefore, cannot be directly related to the effectiveness of thrust generation. The concept of thrust potential, used in the present study to evaluate the propulsive effectiveness of the components of the shcramjet model, addresses this issue by determining how much thrust the engine would develop by taking the difference in momentum between the engine outlet and inlet stations. The outlet momentum is found from a *reversible* expansion of the flow at the station where the thrust potential is to be assessed (subscript b) to an iteratively determined backpressure at the nozzle exit area of the shcramjet (subscript c) [30]. All irreversible losses occurring ahead of station b in the propulsive flow path, due to shocks, mixing processes, and friction, are reflected in the numerically determined magnitude of the flow momentum at that station. Thrust potential $\mathcal{F}_{\mathrm{pot}}$ is thus defined as

$$\mathcal{F}_{\mathrm{pot}} = -\mathcal{F}_{\mathrm{pot,ref}} + \int_b \frac{\rho_c q_c^2 + p_c^\star}{\rho_c q_c} \,\mathrm{d}\dot{m}/\dot{m}_{\mathrm{air,engine}} \tag{12}$$

The reference thrust potential is the negative of the oncoming airflow momentum at the initial cross section of the engine per unit mass of the airflow entering the engine, i.e. $\mathcal{F}_{\mathrm{pot,ref}} = (\rho_0 v_0^2 + p_0)A_0/\dot{m}_{\mathrm{air,engine}} = 3411$ $\mathrm{N \cdot s/kg}$. The initial thrust potential at the initial engine cross section is thus zero.

The propulsive characteristics, such as overall thrust and specific impulse, as well as the magnitudes of the total frictional forces acting on the entire, finite span, engine from tip to tail, were quantified as follows. The thrust of the shcramjet is here determined by the forces acting on its surfaces. The force on the engine walls due to the pressure is taken as the negative of the inviscid momentum terms on the wall surfaces.

$$\mathcal{F}_{p,i} = \sum_{\text{surface nodes}} \Delta X_i[-\boldsymbol{F}_i] \tag{13}$$

where the sum is taken over all surfaces with wall boundary conditions. The term ΔX_i is a directional variable that corresponds to $+1$ or -1 depending whether the normal to the surface is in the positive or negative X_i direction. The skin friction is found as the negative of the viscous momentum on the wall surfaces.

$$\mathcal{F}_{\mathrm{friction},i} = \sum_{\text{surface nodes}} \Delta X_i\left[\sum_{j=1}^{\mathrm{nd}} \mathbf{K}_{i,j}\frac{\partial \mathbf{G}}{\partial X_j}\right] \tag{14}$$

where in both Eqs. (13) and (14) only the momentum components of the vectors on the right side are used. The thrust generated by the fuel entering the engine is determined from its momentum:

$$\mathcal{F}_{\mathrm{fuel},i} = -\Delta X_i(\rho v_i^2 + p)_{\mathrm{fuel}} A_{\mathrm{fuel}} \tag{15}$$

where A_{fuel} is the fuel injection cross-sectional area. The total thrust and lift, which are positive in the $-x_1$ and x_2 directions, respectively, are the sum of the pressure, friction, and fuel thrust forces. The specific impulse I_{sp} can be used for comparison of the performance of different engines.

$$I_{\mathrm{sp}} = \frac{-(\mathcal{F}_{p,1} + \mathcal{F}_{\mathrm{friction},1} + \mathcal{F}_{\mathrm{fuel},1})}{g\dot{m}_{\mathrm{fuel}}} \tag{16}$$

where g is gravitational acceleration. The thrust potential can likewise be converted to an impulse value by multiplying by the mass flow rate of air entering the engine.

$$I_{\mathrm{sp,pot}} = \frac{\mathcal{F}_{\mathrm{pot}}\dot{m}_{\mathrm{air,engine}}}{g\dot{m}_{\mathrm{fuel}}} \tag{17}$$

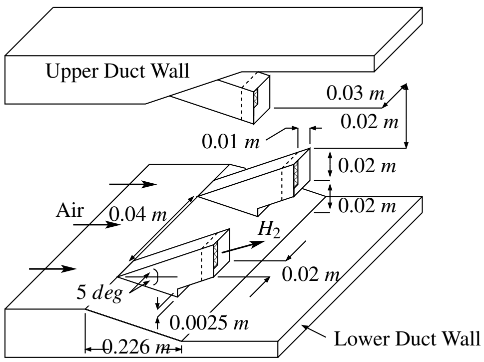

Fig. 2 Cantilevered ramp injector array geometry.

Fuel/Air Premixing in the Inlet

The turbulent mixing process resulting from fuel (hydrogen) injection into the generic mixed-compression inlet airflows by cantilevered ramp injectors has been investigated in detail and reported in [1,4]. In these references, as well as the present paper, the study is limited to a flight Mach number of 11 in the U.S. standard atmosphere [31] at an altitude of 34.5 km. The inflow conditions for the mixed-compression inlet shcramjet, Fig. 1, are thus a pressure of 601 Pa, a temperature of 235 K, and an air velocity of 3391 m/s. The configuration of the cantilevered injector arrays used in the present study is shown in Fig. 2. The arrays are placed on opposite, upper and lower, walls of the internal duct of the mixed-compression inlet in a staggered manner, with a 0.01 m spanwise array displacement and 0.02 m vertical array separation. Details of the inlet geometry and fuel inflow properties are given in Table 1. To maintain consistency with [4], the same restraints on fuel injection conditions are used: a fuel stagnation temperature below 1700 K, static pressure matched to the surrounding air, and a desired convective Mach number greater than one. This necessitates the use of a relatively high global equivalence ratio of 2.7.

The three-dimensional computational domain is 1.26 m long, has a 0.10 m duct height, a 0.03 m width, and has a grid size of $406 \times 248 \times 105 = 10.6$ million cells. A 10-mm-long runway is used inside the fuel injectors before the plane of injection to reduce the solution's sensitivity to the freestream value of ω, which is known to cause difficulties in k-ω schemes. Node spacing at the wall surfaces of 10 μm results in maximum y^+ values of 0.90–3.30. Comparison of similar cases with 10 and 30 μm wall spacing showed a negligible difference in the boundary-layer height or wall shear stress [20]. For the fuel injection flowfields, a limited grid convergence study and subsequent validation of hypervelocity fuel/air mixing processes obtained by the present numerical simulation technique are reported in [4]. Grid-induced errors in integrated properties were estimated to be 10%, with a 14% overestimation of mixing efficiency.

The resulting hydrogen mass fraction distributions are shown in Fig. 3 for x_1 planes through the length of the mixing duct. H_2 mass fraction contours extend exponentially from 0.01 to 1.0, with the stoichiometric mass fraction lying at 0.02876. The corresponding variations in mixing efficiency and thrust potential are depicted in Fig. 4. A detailed analysis of the mixing flow structure in such inlets is reported in [4].

Table 1 Injector geometry, fuel injector parameters, and mixing efficiency

Inlet wedge angle, deg	8.0
Injector compression angle, deg	5.0
Injector expansion angle, deg	5.0
Spanwise array displacement, m	0.01
Vertical array separation, m	0.02
Fuel velocity, m/s	5594
Fuel temperature, K	300
Fuel pressure, Pa	15,000
Fuel density, kg/m^3	0.01202
Convective Mach number	1.24
Global equivalence ratio	2.70
Mixing efficiency, $x_1 = 0.8$ m	0.737
Thrust potential, $\mathrm{N \cdot s/kg}$, $x_1 = 0.8$ m	344

Shcramjet Combustor

The manner in which the oblique detonation wave or shock-induced combustion is generated in a shcramjet combustor can determine whether a shcramjet is viable or not. Shcramjet combustors may use either a turning of the wall or a series of aerodynamic wedges to form standing oblique shock waves that initiate combustion of the premixed fuel and air.

Most studies of shock-induced combustion over aerodynamic wedges assume a homogeneously premixed flow before the combustion-inducing wedge, whereas a few studies, such as that of Cambier et al. [32], assume a more realistic fuel distribution. The realistic flow parameter distribution used in the initial combustor plane of the present work is shown in Fig. 5, which illustrates the temperature and vertical velocity contour plots. The flow illustrated at $x_1 = 0.8$ m ($x_1 = 0.0$ m corresponds to the fuel injection plane in the inlet duct) results from the fuel/air mixing in the internal duct of the inlet by staggered opposed wall cantilevered injectors, for which the H_2 fuel mass fraction is illustrated in Fig. 3e. The fuel is located in the vertical center of the duct, away from the boundary layers along the cowl wall (located at $x_2 = -0.02$ m) and the body wall (located at $x_2 = 0.08$ m). One significant feature of the three-dimensional fuel profile that is not found in prior two-dimensional studies is the fact that there exists an overall streamwise vorticity. This creates a downward velocity of approximately 580 m/s on the right side of Fig. 5b and an upward velocity of approximately 540 m/s on the left side. As such, there will be a variance in strength of any shock created by wedges that span the computational domain.

The use of a single wedge or a deflection of the combustor duct wall is the simplest combustor configuration. Although this results in the "longest" possible combustor configuration, because the combustion-inducing shock must travel the entire height of the duct, it lends itself to mitigation of the recirculation zone, resulting from the shock-induced combustion wave/duct wall boundary-layer interaction. As such, this configuration has been adopted for the present mixed-compression inlet shcramjet model. The wedge angle is 15 deg with a vertical height of 0.04 m resulting in a 0.1493-m-long wedge. The computational grid employed for the combustor is shown in Fig. 6 in which the combustor region extends from $x_1 = 0.80$–0.95 m. At a distance 0.12 m upstream of the start of the combustor, the grid matches that of the inlet mixing duct. In the streamwise direction, 179 cells are used, resulting in 4.7 million nodes. The distance to the first grid point from the wall d_w is 10 μm, resulting in a maximum y^+ that varied from 0.73–6.67.

Figure 7 shows temperature and H_2O mass fraction contours in the spanwise $x_3 = 0.0$, 0.015, and 0.03 m planes, due to ignition and combustion with a single wedge at a distance of 0.80 m from the fuel injection plane. The mixing efficiency in this plane is 0.737. Because the flow contains pure air near the cowl wall, the wedge initially produces a shock that raises the flow temperature to 1200–1500 K. As the shock reaches a vertical location containing premixed H_2 and air, combustion is initiated via a detonation wave (starting at $x_1 \approx 0.84$ m and $x_2 \approx 0$ m in Fig. 7). Variation in the initial flow angle and mixture composition produces a variation in the angle of the detonation wave and determine the distance from the start of the wedge to the combustion front. The hot initial flow produces detonation waves at all cross-sectional locations containing an appropriate fuel/air mixture. The fuel rich flow results in diffusive combustion fronts that propagate downstream as the fuel in the center of the duct burns with the air near the wall surfaces, as observed in the high-temperature bands in Fig. 7.

In an effort to assess the grid-induced error in the shcramjet combustor, a similar combustor configuration and nonhomogeneous inflow is solved with a standard grid density of $201 \times 280 \times 105 = 5.9$ million grid cells. The grid density is similar to that used for the combustor results presented, but on a

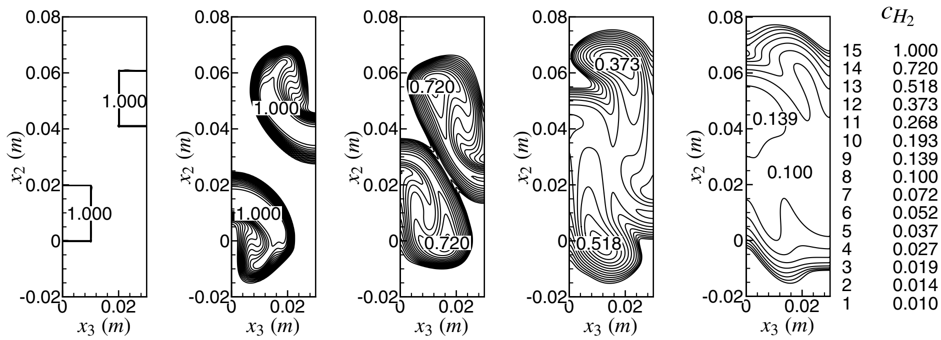

a) $x_1 = 0$ *m* b) $x_1 = 0.2$ *m* c) $x_1 = 0.4$ *m* d) $x_1 = 0.6$ *m* e) $x_1 = 0.8$ *m*

Fig. 3 Hydrogen mass fraction contours in inlet.

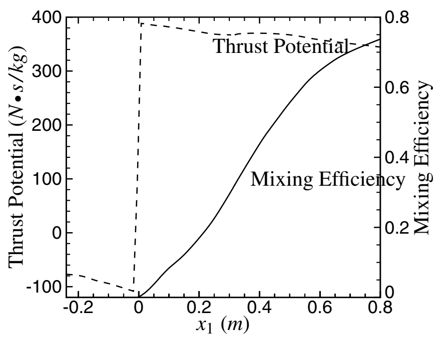

Fig. 4 Performance parameters for fuel/air premixing.

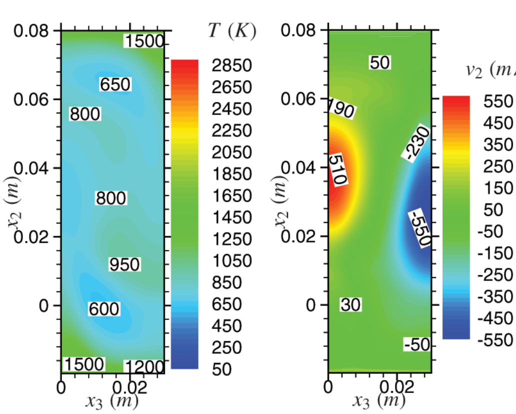

a) Temperature **b) Vertical velocity**

Fig. 5 Flow properties at the combustor entrance of the mixed-compression inlet shcramjet, $x_1 = 0.80$ m.

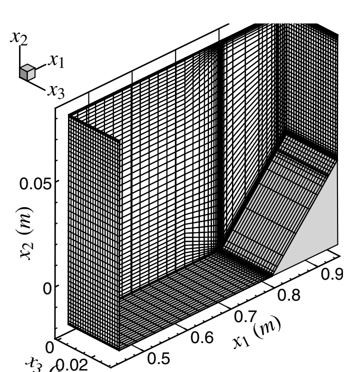

Fig. 6 Combustor numerical grid (every fifth node shown).

slightly different streamwise domain. The solution was also determined on a coarse grid with half the number of nodes in each dimension (0.7 million) and on a fine grid with double the number of nodes in each dimension (47.2 million). Figure 8 illustrates the temperature variation along a streamline in the $x_3 = 0.0$ m plane originating at $x_1 = 0.55$ m and $x_2 = 0.0$ m for each of the three grid densities. The greater the grid density, the farther downstream the shock and detonation wave are initiated. For the streamline shown in Fig. 8, there is a maximum difference in temperature between the coarse and standard grid of 11% (195 K) and between the standard and fine grid of 4% (81 K). The maximum temperature reached through the detonation wave is within 0.3% (6 K) for all grid densities. Similar trends are found in the rest of the flowfield. Integrated values are influenced by the slight delay in the combustion process on the finer grid densities, with the thrust potential increase occurring slightly downstream. The regular grid density provides a 0.6% greater maximum thrust potential than the fine and coarse grid density cases that have the same value.

The general behavior of the flow generated by the wedge-induced shock confined in a duct is shown in the pressure contour field around a wedge in Fig. 9. A flow recirculation region is found on the upper duct wall where the bow shock impinges and reflects from the wall. In the present case, the three-dimensional nature of the flow with variations in the detonation wave strength across the combustor span results in a detonation wave/boundary-layer interaction generated recirculation zone of varying intensity and flow angles behind the wave ranging from 14 to 19 deg. To eliminate the detrimental effects of the recirculation region on the combustor and engine performance as a whole, two methods were used to reduce the recirculation region. The first was to expand the combustor flow into the nozzle as the detonation wave reaches the body wall. The second was to inject air parallel to the x_1 axis through a 0.004-m-high slot in the combustor upper wall at $x_1 = 0.93$ m. The air had a temperature of 500 K (matching the prescribed wall temperature), a pressure of 5000 Pa (approximately a quarter that of the surrounding combustible mixture), and a velocity of 2000 m/s, resulting in an air mass flow rate of 0.084 kg/s. An additional 44 grid cells were added in the x_2 direction for the simulation of the air injection and subsequent downstream flow. Because the strength of the detonation wave/wall boundary-layer interaction varies in the computational span, this injectant mass flow rate does not entirely eliminate the recirculation region. The resulting small recirculation zone varies in size across the computational domain, with length along the wall ranging between 0.0052–0.007 m and height perpendicular to the wall ranging from 0.0011–0.0019 m, Fig. 10. The recirculation zone does not create flow blockage in the combustor, but acts to compress the injected air flow.

Expansion System

The shock-induced combustion products are expanded in the nozzle. For purposes of configuring the nozzle surfaces, the three-dimensional reacting exhaust flow is assumed to be chemically frozen and inviscid, and the two-dimensional method of character-

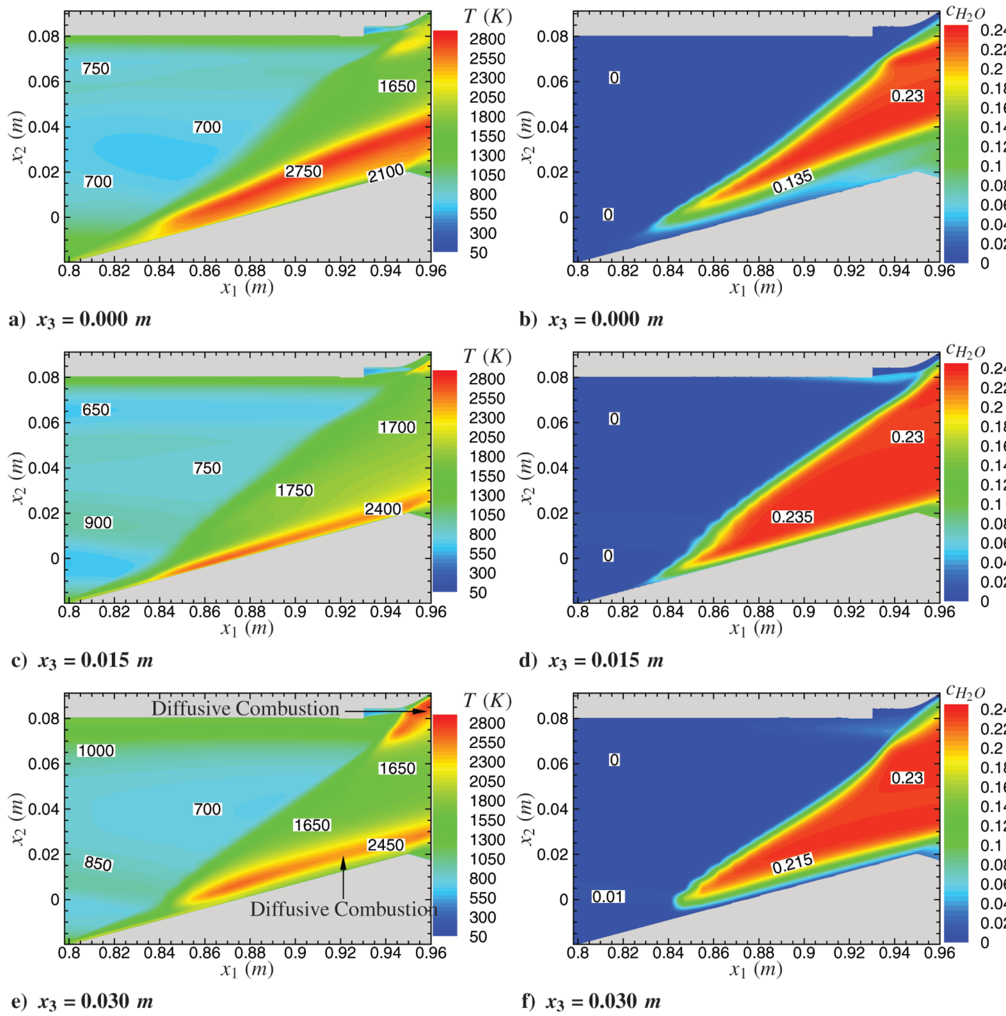

Fig. 7 Temperature and H_2O mass fraction contours at different spanwise x_3 planes.

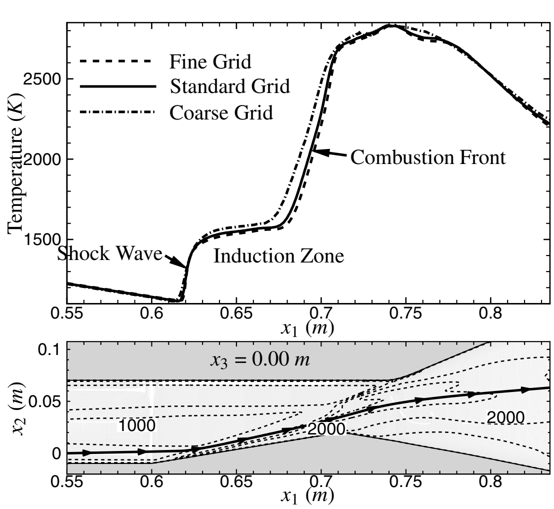

Fig. 8 Grid convergence of temperature along a streamline.

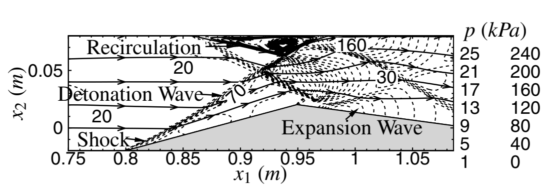

Fig. 9 Flow behavior of confined shock-induced combustion in two-dimensional duct.

istics (MOC) for rotational flows is used to construct the upper and lower contours of the nozzle in a plane. The MOC is subject to the following conditions: the exhaust gases are directed parallel to the flight direction, to recover maximum thrust, and the exit pressure is determined (iteratively) to terminate the nozzle upper wall at the top surface of the shcramjet to avoid unnecessary drag. The initial data line for the MOC is located longitudinally at the end of the combustor and spanwise at the $x_3 = 0.03$ m computational symmetry plane. The dual wall technique [33–36] was used for determining the nozzle walls. Because the resulting nozzle wall contours were exceedingly long, they were truncated to provide 95–98% of their maximum thrust, to reduce frictional drag and weight, resulting in a nozzle that was 30% the length of the MOC generated contour. To account for the development of the turbulent boundary layers on the nozzle

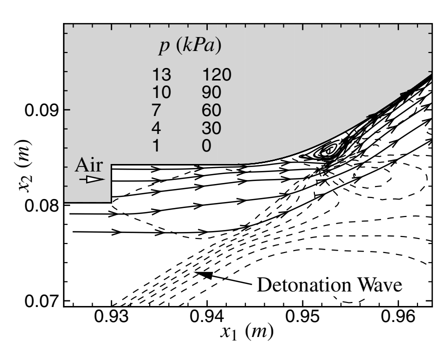

Fig. 10 Detonation wave/boundary-layer recirculation with air injection in the $x_3 = 0.015$ m plane.

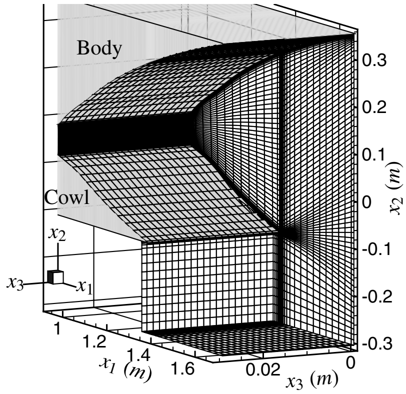

Fig. 11 Numerical grid for mixed-compression shcramjet (every fifth node shown).

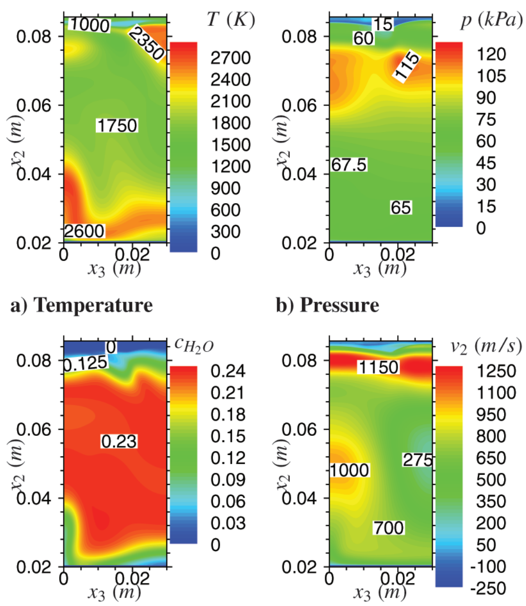

a) Temperature b) Pressure

c) Water mass fraction d) Vertical velocity

Fig. 12 Flow properties at the nozzle entrance, $x_1 = 0.95$ m.

walls, Edenfield's [37] experimental correlations were used to determine the displacement thickness, which was then used to adjust the MOC-obtained contours by a vertical distance, such that the viscous flow matches the inviscid contour mass flow rate. The nozzle and cowl wall contours thus generated in the $x_3 = 0.03$ m plane were assumed to prevail over the entire lateral span of the three-dimensional computational domain. The outer surface of the cowl was contoured by a third-degree polynomial passing through the cowl leading and trailing edges, forming at these points inclusion angles of 5 deg.

The entire three-dimensional reacting nozzle flowfield continuing that from the combustor, as well as the flow around the outer cowl surface, were then numerically simulated using the WARP code. The flow outside the cowl was determined by two-dimensional simulation up to a distance of 0.30 m before the trailing edge of the cowl, thereafter the interaction with the inner reacting flow and the flow past the cowl trailing edge was treated as three-dimensional and solved simultaneously with the inner nozzle flow.

The dimensions of the computational domain and the grid used for the expansion flow simulation are as follows. The nozzle begins at $x_1 = 0.95$ m and extends vertically from $x_2 = 0.02$ to 0.08 m. The three-dimensional flow region outside the cowl begins at $x_1 = 1.329$ m and extends vertically from $x_2 = -0.30$ to -0.11 m. The inner and outer flows combine at the trailing edge of the cowl, $x_1 = 1.363$ m, and, by the end of the nozzle at $x_1 = 1.69$ m, the

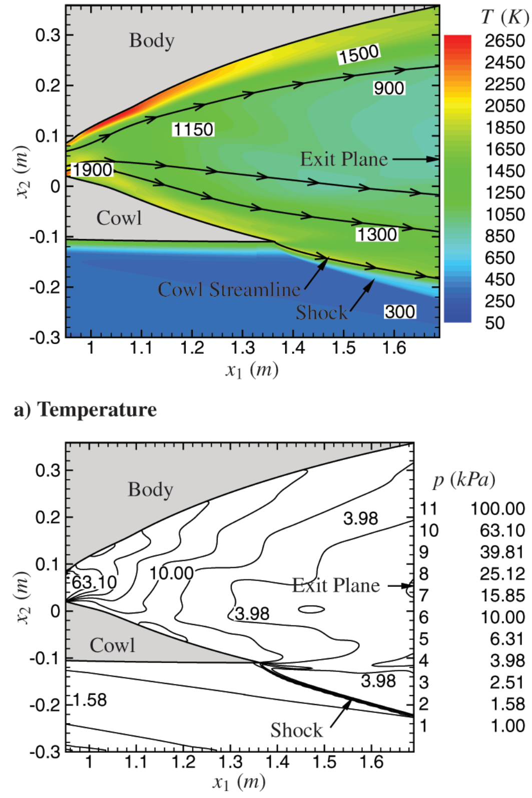

a) Temperature

b) Pressure

Fig. 13 Nozzle flow properties, $x_3 = 0.015$ m.

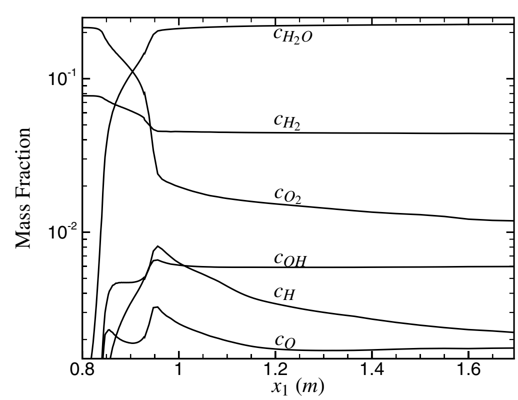

Fig. 14 Change in average species mass fractions through combustor and nozzle.

flowfield covers a vertical distance of $x_2 = -0.30$ to 0.36 m. The computational grid was matched to that of the combustor with 292 cells in the x_2 direction and 105 cells in the x_3 direction at the initial plane of the inner reacting flow. An additional 90 cells are used in the x_2 direction for the grid of the outer cold flow region. In the x_1 direction, 178 cells were used from the beginning of the nozzle to its end. The entire three-dimensional computational grid contained both the combustor and nozzle and thus contained 9.3×10^6 cells. The grid in the nozzle is shown in Fig. 11.

The start of the nozzle expansion is located at the x_1 station near where the thrust potential in a straight duct reaches its maximum due to the combustion process. Figure 12 depicts the variations of the flow variables in this plane. For $d_w = 10$ μm, the maximum y^+ is 0.91–4.52 on the upper nozzle wall, 1.00–1.82 at the lower nozzle wall, and 0.11–1.15 at the outer cowl wall.

The obtained nozzle configuration, as well as the behavior of the three-dimensional reacting flowfield resulting from the expansion of the shock-induced combustion products, are depicted in Fig. 13. The

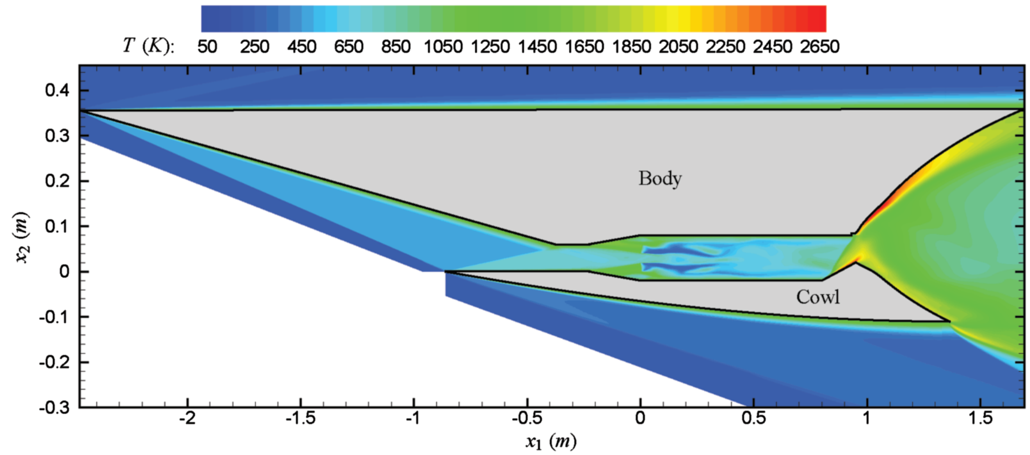

Fig. 15 Temperature contours in the mixed-compression inlet shcramjet, $x_3 = 0.015$ m.

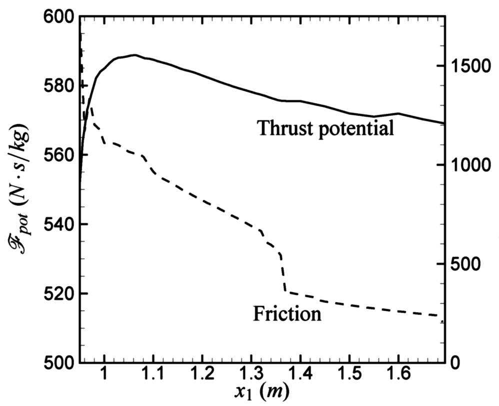

Fig. 16 Variation of thrust potential and frictional forces in the x_1 direction through the nozzle.

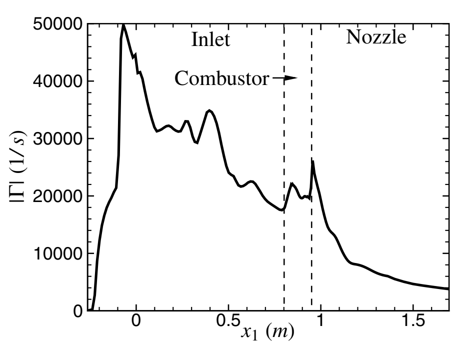

Fig. 17 Absolute value of the circulation.

Mach number at the nozzle exit is approximately four, as compared with the flight Mach number of 11, and the average nozzle exit velocity is 3423 m/s for a flight velocity of 3391 m/s. Because the nozzle was truncated in length, the exit plane flow is not parallel to the x_1 axis, but expands outward with angles ranging from -10.4 to 17.8 deg. Because of significant pressure differences between the inner flow and the flow outside the cowl, a shock is formed at the trailing edge of the cowl. Figure 14 illustrates the average H_2O, O, OH, H, and O_2 mass fraction variations. The bulk of the combustion takes place in the combustor, however, additional diffusive burning occurs in the nozzle at the fuel/air interfaces near both the upper and lower nozzle walls, and through recombination processes, as is evident from the decrease in c_O and c_H. These additional combustion processes increase the H_2O mass fraction by 15% from the end of the combustor to the nozzle exit, contributing to the thrust of the engine.

The temperature contours in the center symmetry plane, $x_3 = 0.015m$, for the entire shcramjet flowfield, are presented in Fig. 15. The mass flow through the engine resides above the streamline and shear layer originating from the end of the cowl, and can be seen to cover an exit plane height of 0.544 m, which is 53% larger than the inlet airflow capture height. Similar expansion is observed in all spanwise planes, with exit plane heights of 0.542–0.546 m. Figure 16 depicts the variation of the thrust potential and of the frictional forces on the walls of the nozzle. The thrust potential initially increases due to continued combustion processes at the start of the nozzle expansion and subsequently decreases, due to frictional forces, to 3% above the level at the start of the nozzle. The sum total of the frictional forces acting on the nozzle walls is 13.8 N. No attempt has been made to assess the effect of nozzle wall temperature on its performance.

Figure 17 presents the variation of the absolute value of circulation along the streamwise x_1 direction. The significant vorticity is initially generated by cross-stream shear and baroclinic torque around the fuel injector structures. This vorticity subsequently declines through the inlet mixing duct with undulating variations of vorticity caused by intersection of the fuel carrying vortices and shock waves reflected from the walls of the duct. The shock generated by the aerodynamic wedge increases the streamwise vorticity in the flow. The combustion-inducing shock starts at $x_1 = 0.8$ m and generates a 35% increase in the absolute value of the circulation. The expansion process through the nozzle destroys most of the vortical behavior of the flow with the absolute value of the circulation declining sharply through the nozzle.

Propulsive Performance

Pressure and frictional forces are considered on all wetted surfaces of the hypersonic engine (between the two lateral boundaries of the computational domain of the infinite span engine considered). The frictional forces are most significant in the combustor and constitute approximately 15% of the frictional drag, whereas the combustor length is only 4% of the total engine length. Moreover, the shock-inducing wedge generates 71% of the drag due to pressure forces and 48% of the total drag. Thrust potential losses in the inlet and mixing duct are -152 $N \cdot s/kg$, not counting the 502 $N \cdot s/kg$ gain from the thrust of the fuel injection, whereas the combustor and nozzle system provide a thrust potential gain of 219 $N \cdot s/kg$.

Table 2 Geometrical dimensions and shcramjet performance parameters

Length, m	4.170	$\mathcal{F}_{\mathrm{friction},1}$, N	65.77
Height, m	0.465	$\mathcal{F}_{\mathrm{thrust}}$, N	197.59
Span, m	0.03	I_{sp}, s	683
$\dot{m}_{\mathrm{air}}$, kg/s	0.319	I_{sp} (engine), s	803
$\dot{m}_{\mathrm{fuel}}$, kg/s	0.02690	$I_{\mathrm{sp,\,pot}}$ (engine), s	783

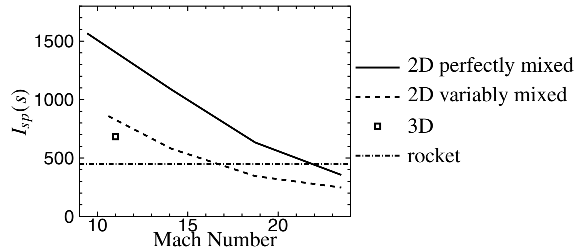

Fig. 18 Hypersonic engine specific impulse with Mach number (curves from [38]).

Table 2 summarizes the geometrical dimensions, global fuel/air injection parameters used, and the propulsive performances characteristics of the considered shcramjet. Actual overall thrust and fuel specific impulse, as well as the "potential" specific impulse, calculated from the thrust potential, are presented. The fuel specific impulse I_{sp} is determined for the entire vehicle, whereas the "engine" value stands for the fuel specific impulse due solely to the internal flow path in the engine and is comparable to the $I_{sp,pot}$ value. The I_{sp} value does not include the thrust generated via the air slot injection in the combustor as it is assumed that the air flow is reversibly routed from the inlet air flow.

In [38], where an inviscid reacting flow simulation was employed to study the effects of incomplete fuel/air mixing on the propulsive performance of a two-dimensional mixed-compression inlet shcramjet at different flight Mach numbers, it was estimated that the fuel specific impulse for a flight Mach number of 11 would lie between approximately 830 s for a highly inhomogeneous fuel/air mixture and 1130 s in the case of a homogeneous mixture, Fig. 18. Although the shcramjet configuration considered in the present study is not exactly the same as that in [38], the fuel specific impulse of 683 s found in the current study, with the added complexities of a realistic solution, is in keeping with those given in [38].

Conclusions

A shock-induced combustion ramjet was considered with gaseous hydrogen injected by cantilevered ramp injectors mounted in a staggered manner on the upper and lower walls at the upstream end of the internal mixing duct of a generic mixed-compression inlet of the engine. It was shown, by numerical simulation of the three-dimensional turbulent fuel/air mixing flowfield, that the combustible mixture was well away from the confining upper and lower duct walls. A relatively high value of 0.737 for the mixing efficiency was obtained for a fuel equivalence ratio of 2.7, considering the very high air and fuel velocities prevailing in the mixing duct (3391 and 5596 m/s, respectively). The products of the shock-induced combustion wave generated by a wedge located downstream on the lower wall of the mixing duct were expanded in a specifically designed nozzle. Magnitudes of the thrust, fuel specific impulse, and frictional forces acting on the entire shcramjet were determined by numerical simulation of the complete three-dimensional shcramjet flowfield. The obtained value of the specific impulse of 683 s is moderate due to the high equivalence ratio employed. Further optimization of the fuel/air mixing strategy should further improve the fuel specific impulse of the considered shcramjet engine model.

References

[1] Sislian, J. P., and Parent, B., "Hypervelocity Fuel/Air Mixing in a Shcramjet Inlet," *Journal of Propulsion and Power*, Vol. 20, No. 2, 2004, pp. 263–272.

[2] Sislian, J. P., Martens, R., Schwartzentruber, T. E., and Parent, B., "Numerical Simulation of a Real Shcramjet Flowfield," *Journal of Propulsion and Power*, Vol. 22, No. 5, 2006, pp. 1039–1048. doi:10.2514/1.14895

[3] Vinogradov, V. A., Shikhman, Y. M., and Segal, C., "Review of Fuel Pre-Injection Studies in a High-Speed Airflow," *44th AIAA Aerospace Sciences Meeting and Exhibit*, AIAA Paper 2006-1030, Jan. 2006.

[4] Alexander, D. C., Sislian, J. P., and Parent, B., "Hypervelocity Fuel/Air Mixing in Mixed-Compression Inlets of Shcramjets," *AIAA Journal*, Vol. 44, No. 10, 2006, pp. 2145–2155. doi:10.2514/1.12630

[5] Alexander, D. C., "Hypersonic Mixed-Compression Inlet Shock-Induced Combustion Ramjets," Ph.D. Thesis, Graduate Dept. of Aerospace Science and Engineering, Univ. of Toronto, Toronto, 2006.

[6] Wilcox, D. C., "Reassessment of the Scale Determining Equation for Advanced Turbulence Models," *AIAA Journal*, Vol. 26, No. 11, 1988, pp. 1299–1310.

[7] Jachimowski, C. J., "An Analytical Study of Hydrogen-Air Reaction Mechanism with Application to Scramjet Combustion," NASA TP 2791, 1988.

[8] McBride, B. J., and Reno, M. A., "Coefficients for Calculating Thermodynamic and Transport Properties of Individual Species," NASA TM 4513, 1993.

[9] Dimotakis, P. E., *Turbulent Free Shear Layer Mixing and Combustion*, AIAA, Washington, DC, 1991, pp. 265–340.

[10] Papamoschou, D., and Roshko, A., "Compressible Turbulent Shear Layer: An Experimental Study," *Journal of Fluid Mechanics*, Vol. 197, Dec. 1988, pp. 453–477. doi:10.1017/S0022112088003325

[11] Wilcox, D. C., "Dilatation-Dissipation Corrections for Advanced Turbulence Models," *AIAA Journal*, Vol. 30, No. 11, 1992, pp. 2639–2646.

[12] Coakley, T. J., Horstman, C. C., Marvin, J. G., Viegas, J. R., Bardina, J. E., Huang, P. G., and Kussoy, M. I., "Turbulent Compressibility Corrections," NASA TM 108827, May 1994.

[13] Parent, B., and Sislian, J. P., "Use of Domain Decomposition in Accelerating the Convergence of Quasihyperbolic Systems," *Journal of Computational Physics*, Vol. 179, No. 1, 2002, pp. 140–169. doi:10.1006/jcph.2002.7048

[14] Roe, P. L., "Approximate Riemann Solvers, Parameter Vectors, and Difference Schemes," *Journal of Computational Physics*, Vol. 43, No. 2, 1981, pp. 357–372. doi:10.1016/0021-9991(81)90128-5

[15] Yee, H. C., Klopfer, G. H., and Montagné, J. L., "High-Resolution Shock-Capturing Schemes for Invisid and Viscous Hypersonic Flows," *Journal of Computational Physics*, Vol. 88, No. 1, 1990, pp. 31–61. doi:10.1016/0021-9991(90)90241-R

[16] Beam, R. M., and Warming, R. F., "An Implicit Factored Scheme for the Compressible Navier–Stokes Equations," *AIAA Journal*, Vol. 16, No. 4, 1978, pp. 393–402.

[17] Chang, C. L., and Merkle, C. L., "Relation Between Flux Vector Splitting and Parabolized Schemes," *Journal of Computational Physics*, Vol. 80, No. 2, 1989, pp. 344–361. doi:10.1016/0021-9991(89)90104-6

[18] Coakley, T. J., and Huang, P. G., "Turbulent Modelling for High-Speed Flows," AIAA Paper 92-04366, 1992.

[19] Batten, P., Leschziner, M. A., and Goldberg, U. C., "Average-State Jacobians and Implicit Methods for Compressible Viscous and Turbulent Flows," *Journal of Computational Physics*, Vol. 137, No. 1, 1997, pp. 38–78. doi:10.1006/jcph.1997.5793

[20] Parent, B., Sislian, J. P., and Schumacher, J., "Numerical Investigation of the Turbulent Mixing Performance of a Cantilevered Ramp Injector," *AIAA Journal*, Vol. 40, No. 8, 2002, pp. 1559–1566.

[21] Settles, G. S., Vas, I. E., and Bogdonoff, S. M., "Details of a Shock-Separated Turbulent Boundary Layer at a Compression Corner," *AIAA Journal*, Vol. 14, No. 12, 1976, pp. 1709–1715.

[22] Burrows, M. C., and Kurkov, A. P., "Analytical and Experimental Study of Supersonic Combustion of Hydrogen in a Vitiated Air Stream," NASA TMX 2828, 1973.

[23] Waitz, I. A., Marble, F. E., and Zukoski, E. E., "Investigation of a Contoured Wall Injector for Hypervelocity Mixing Augmentation," *AIAA Journal*, Vol. 31, No. 6, 1993, pp. 1014–1021.

[24] Donohue, J. M., McDaniel, J. C., Jr., and Haj-Hariri, H., "Experimental and Numerical Study of Swept Ramp Injection into a Supersonic Flowfield," *AIAA Journal*, Vol. 32, No. 9, 1994, pp. 1860–1867.

[25] Mao, M., Riggins, D. W., and McClinton, C. R., "Numerical Simulation of Transverse Fuel Injection," NASA Paper N91-21062 13-02, presented at the CFD Symposium on Aeropropulsion, NASA Lewis Research Center, 1991.

[26] Lehr, H. F., "Experiments in Shock-Induced Combustion," *Astronautica Acta*, Vol. 17, Nos. 4–5, 1972, pp. 589–597.

[27] Parent, B., and Sislian, J. P., "Validation of Wilcox k-ω Model for Flows Characteristic to Hypersonic Airbreathing Propulsion," *AIAA Journal*, Vol. 42, No. 2, 2004, pp. 261–270.

[28] Wilcox, D. C., *Turbulence Modeling for CFD*, 2nd ed., DCW Industries, La Cañada, CA, 1998.

[29] Schwartzentruber, T. E., Sislian, J. P., and Parent, B., "Suppression of Premature Ignition in the Premixed Inlet Flow of a Shcramjet," *Journal of Propulsion and Power*, Vol. 21, No. 1, 2005, pp. 87–94.

[30] Parent, B., and Sislian, J. P., "Effect of Geometrical Parameters on the Mixing Performance of Cantilevered Ramp Injectors," *AIAA Journal*, Vol. 41, No. 3, 2003, pp. 448–456.

[31] *U.S. Standard Atmosphere*, U.S. Government Printing Office, Washington, DC, 1976.

[32] Cambier, J., Adelman, H., and Menees, G. P., "Numerical Simulations of an Oblique Detonation Wave Engine," *Journal of Propulsion and Power*, Vol. 6, No. 3, 1990, pp. 315–323.

[33] Hammer, S. S. and Agosta, V. D., "Scramjet Nozzle Analysis," PSI R-70-1, Propulsion Sciences, Melville, NY, 1970.

[34] Migal, D., "Supersonic Annular Nozzles," *Journal of Spacecraft and Rockets*, Vol. 9, No. 1, 1972, pp. 3–6.

[35] Veen, R. V., Gentry, R., and Hoffman, J. D., "Design of Shrouded-Plug Nozzles for Maximum Thrust," *AIAA Journal*, Vol. 12, No. 9, 1974, pp. 1193–1197.

[36] Park, H.-K., "Model of an Aerospace Plane Based on an Idealized Cone-Derived Waverider Forebody," Ph.D. Thesis, Univ. of Oklahoma, Norman, OK, 1990.

[37] Edenfield, E. E., "Design of a High Reynolds Number Mach Number 8 Contoured Nozzle for the Hypervelocity Wind Tunnel," Arnold Engineering Development Center TR 72-48, Aug. 1972.

[38] Sislian, J. P., Dudebout, R., Schumacher, J., Islam, M., and Redford, T., "Incomplete Mixing and Off-Design Effects on Shock-Induced Combustion Ramjet Performance," *Journal of Propulsion and Power*, Vol. 16, No. 1, 2000, pp. 41–48.

J. Powers
Associate Editor